




 Cite this: *RSC Adv.*, 2019, 9, 28569

In situ mass change and gas analysis of 3D manganese oxide/graphene aerogel for supercapacitors†

 Phansiri Suktha,^{ab} Poramane Chiochan,^{ab} Atiweena Krittayavathananon,^{ab}
Sangchai Sarawutanukul,^{ab} Sathyamoorthi Sethuraman ^{ab}
and Montree Sawangphruk ^{*ab}

Manganese oxide nanoparticles decorated on 3D reduced graphene oxide aerogels (3D MnO_x/rGO_{ae}) for neutral electrochemical capacitors were successfully produced by a rapid microwave reduction process within 20 s. The symmetric electrochemical capacitor of 3D MnO_x/rGO_{ae} (Mn 3.0 at%) storing charges *via* both electric double layer capacitance (EDLC) and pseudocapacitance mechanisms exhibits a specific capacitance of 240 F g⁻¹ as compared with 190 F g⁻¹ of that using the bare 3D rGO_{ae} at 0.5 A g⁻¹ in 1 M Na₂SO₄ (aq.) electrolyte. It retains 90% of the initial capacitance after 10 000 cycles, demonstrating high cycling stability. In addition, the charge storage mechanism of 3D MnO_x/rGO_{ae} was investigated using an electrochemical quartz crystal microbalance. *In situ* gas analysis using differential electrochemical mass spectrometry (DEMS) shows the CO₂ evolution at a cell potential over 1 V indicating that the positive electrode is possibly the voltage limiting electrode in the full cell. This finding may be useful for further development of practical high power and energy supercapacitors.

 Received 16th July 2019
Accepted 4th September 2019

DOI: 10.1039/c9ra05444h

rsc.li/rsc-advances

Introduction

Electrochemical capacitors or supercapacitors (SCs) have attracted interest because of their high specific power, high charging–discharging rate, and long cycling stability.^{1–3} SCs can be classified by their charge storage mechanisms such as electrical double layer capacitor (EDLC) and pseudocapacitors. Generally, carbon-based materials are widely used as active materials in EDLCs storing charges by the electrosorption of ions on their surfaces. In contrast, pseudocapacitors store charge *via* redox reaction at the solid–liquid interface or the intercalation of ions at the surface.⁴ The conducting polymers and metal oxides are widely used as pseudocapacitive materials. Among them, manganese oxide is one of the best electrode materials for supercapacitors due to its good stability, low cost, natural abundance, and environmentally friendly nature.^{5,6} However, it has poor electrical conductivity (10⁻⁵ to 10⁻⁶ S cm⁻¹).⁷ Therefore, it is usually combined with highly conductive carbon-based material such as carbon nanotube

(CNT), carbon fibre, and graphene or reduced graphene oxide (rGO) to improve its electrochemical performance.^{2,8–10}

Graphene is widely used as supercapacitor electrode material due to its high electrical conductivity and high specific surface area.^{11,12} There are many reports relating to reduced graphene oxide/manganese oxide (rGO/MnO_x) composites as supercapacitor electrodes. For example, the rGO/Mn₃O₄ composite produced by a hydrothermal process exhibits a specific capacitance of 121 F g⁻¹ at 0.5 A g⁻¹ in 1 M Na₂SO₄.¹³ Nitrogen doped graphene/Mn₃O₄ produced by the hydrothermal process shows a specific capacitance of 205 F g⁻¹ at 1.0 A g⁻¹.¹⁴ The rGO/Mn₃O₄ prepared by the N₂ dielectric barrier discharge plasma exhibits a specific capacitance of 193 F g⁻¹, while the specific capacitance of pure Mn₃O₄ is only 95 F g⁻¹.¹⁵ Recently, 3D graphene has attracted interest because the 3D interconnected structure of graphene sheets can increase ion mobility and electron transport.¹⁶ For example, the graphene hydrogel shows a specific capacitance of 190 F g⁻¹ at 0.5 A g⁻¹ in 6 M KOH.¹⁷ 3D rGO produced by the chemical reduction method shows a specific capacitance of 204 F g⁻¹ at 0.5 A g⁻¹ in 6 M KOH.¹⁸ 3D graphene network shows a specific capacitance of 190 F g⁻¹ at 0.5 A g⁻¹ in 6 M KOH.¹⁹ The specific capacitance of 3D graphene aerogel is 245 F g⁻¹ at 1.0 A g⁻¹ in PVA/H₃PO₄ solid electrolyte.²⁰

In this work, we further developed the supercapacitor electrode using the 3D manganese oxide/reduced graphene oxide aerogel (MnO_x/rGO_{ae}) composite synthesized by a microwave reduction method. This technique is facile, effective, rapid, and

^aDepartment of Chemical and Biomolecular Engineering, School of Energy Science and Engineering, Vidyasirimedhi Institute of Science and Technology, Rayong 21210, Thailand. E-mail: Montree.s@vistec.ac.th

^bCentre of Excellence for Energy Storage Technology (CEST), Vidyasirimedhi Institute of Science and Technology, Rayong 21210, Thailand

† Electronic supplementary information (ESI) available: EDS spectra, electrochemical performance and comparison table of rGO/MnO_x composites. See DOI: 10.1039/c9ra05444h



environmentally friendly.^{21–25} The 3D MnO_x/rGO_{ae} can store charges *via* the EDLC of 3D rGO_{ae} and the surface redox of MnO_x leading to high power and energy. The charge storage mechanism of ion sorption was investigated by the electrochemical quartz crystal microbalance (EQCM) and *in situ* gas analysis using the differential electrochemical mass spectroscopy (DEMS). The DEMS can also provide the working potential limit without the gas evolution, which is a root of the poor stability of supercapacitors. The electrochemical performance of the symmetrical neutral supercapacitors using four composites with different MnO_x loading contents. The symmetric electrochemical capacitor of 3D MnO_x/rGO_{ae} (Mn 3.0 at%) exhibits a specific capacitance of 240 F g^{−1} as compared with 190 F g^{−1} of that using the bare 3D rGO_{ae} at 0.5 A g^{−1} in 1 M Na₂SO₄ (aq.) electrolyte.

Experimental

Chemicals and materials

Graphite powder (<20 μm, Aldrich), sodium nitrate (NaNO₃, 99% Ajax Finechem), potassium permanganate (KMnO₄, 99%, UNIVAR), sulphuric acid (H₂SO₄, 98%, QRec), nitric acid (HNO₃, 65%, QRec), hydrogen peroxide (H₂O₂, 30%, Chem Supply), hydrochloric acid (HCl, 37%, QRec), ethanol (99.9%, QRec), polyvinylidene fluoride (PVDF, *M_w* ~ 534 000, Sigma-Aldrich), carbon black (99+%, Super P), (*N*-methyl-2-pyrrolidone) (NMP, 99.5% QRec), and sodium sulfate (Na₂SO₄ 99%, CARLO ERBA) were analytical reagent grade and used without further purification. Carbon fibre paper (CFP) was from SGL CARBON SE, Germany. Deionized water from Millipore system (DI water, 15 MΩ cm) was used in all experiments.

Synthesis of graphene oxide aerogel

Graphene oxide (GO) was synthesised using a modified Hummer's method. Briefly, 5.0 g graphite powder and 7.5 g NaNO₃ were mixed in 500 mL conc. H₂SO₄ in an ice-bath keeping the temperature below 20 °C. 40 g KMnO₄ was slowly added into the mixture and stirred for 24 h at an ambient temperature. Then, 500 mL DI water and 150 mL H₂O₂ were subsequently added into the mixture and kept stirring for 24 h. The mixture was washed with 5% HCl and then centrifuged with DI water for several times until neutral.²⁶ Finally, the obtained product was then washed with DI water for several times and freeze-dried for 72 h.

Synthesis of MnO_x/rGO_{ae} composite

0.42 g GO aerogel was dispersed in 30 mL KMnO₄ (0.088 M) solution with varying weight of GO : KMnO₄ (1 : 1, 2 : 1, 4 : 1, and 8 : 1 by weight) becoming the suspension. Then, 0.25 mL ethanol was added into the suspension under constant magnetic stirring and then further stirred for 4 h at room temperature.²⁷ Then, the GO/MnO_x was filtered, washed with deionized water and ethanol, and dried at 60 °C for 24 h. The MnO_x/GO was heated by a microwave reduction method at a power of 200 W for 20 s to obtain MnO_x/rGO_{ae}. Finally, the obtained product was then dried at 80 °C for 24 h. The rGO_{ae}

was synthesised by the microwave method at 200 W using GO aerogel precursor.

Fabrication of MnO_x/rGO_{ae} composite electrodes

Active material powder (8 mg), carbon black (CB) using as a conductive additive (1 mg), and PVDF using as a binder (1 mg) were dispersed and sonicated in *N*-methyl-2-pyrrolidone (NMP, 1 mL) solvent. The as-prepared carbon slurry was then drop-coated on the functionalized-carbon fibre paper (f-CFP) with a diameter of 1.58 cm. The mass loading was about 1 mg cm^{−2}. The electrode was dried at 80 °C for 24 h. The hydrolysed polyethylene (PE) film and 1 M Na₂SO₄ (aq.) were used as a separator and an electrolyte, respectively. Prior to the fabrication of supercapacitor, the separator was soaked in the electrolyte for 10 min. The symmetric supercapacitors were assembled in 2016-type coin cells using a hydraulic compression machine at 800 psi for the evaluation of electrochemical performance. Whilst, 2032-type coin cells with the hole were used for *in situ* gas analysis using DEMS. The CV was carried out at 10 mV s^{−1} up to the gas evolution with the pre-defined voltage intervals. For EQCM measurement, the carbon slurry was drop-coated on Au support (0.67 cm in diameter) about 0.22 mg cm^{−2}. Ag/AgCl (3 M KCl) with gel electrolyte and Au wire were used as reference electrode and counter electrode, respectively.

Characterization

The morphologies of as-synthesised materials were characterized by FE-SEM/EDS (FE-SEM, JEOL JSM-7610F), and TEM (TEM, Hitachi HT7700). The crystalline structure was characterized by XRD (Bruker D8 ADVANCE using Cu-Kα radiation (λ = 1.5418 Å)). The chemical structure was characterized by FTIR (PerkinElmer) and Raman spectroscopy (Bruker, an excitation wavelength of 532 nm). The specific surface area was measured by nitrogen adsorption/desorption with the BET method (BELSORP-mini, MicrotracBEL). The surface composition was analysed by X-ray photoelectron spectroscopy (XPS, JEOL, JSP-9010MC). *In situ* gas detection was carried out by DEMS (Hiden analytical, HPR-40). Cyclic voltammetry (CV) and galvanostatic charge–discharge measurement (GCD) were performed using a Metrohm AUTOLAB potentiationstat (PGSTAT 302N) and battery tester (Neware, Gelon, HongKong), respectively.

Results and discussion

The morphologies of rGO_{ae} and MnO_x/rGO_{ae} composites were characterized by FE-SEM as shown in Fig. 1. The rGO_{ae} shows a 3D sponge like structure with the interconnected graphene sheets and macroporous voids (inset image in Fig. 1a). Spherical MnO_x nanoparticles decorated on the graphene nano-sheet are observed for MnO_x/rGO_{ae} composite (8 : 1 GO : KMnO₄ ratio) (Fig. 1a). The number of nanoparticles decorated on the graphene nanosheet increase with increasing the concentration of Mn source for the synthesis of MnO_x/rGO_{ae} composite. For example, the dense nanoparticle coverage on the graphene sheet is observed for 1 : 1 GO : KMnO₄ ratio. It may decrease the total surface area and pore volume of the composite. Also, the



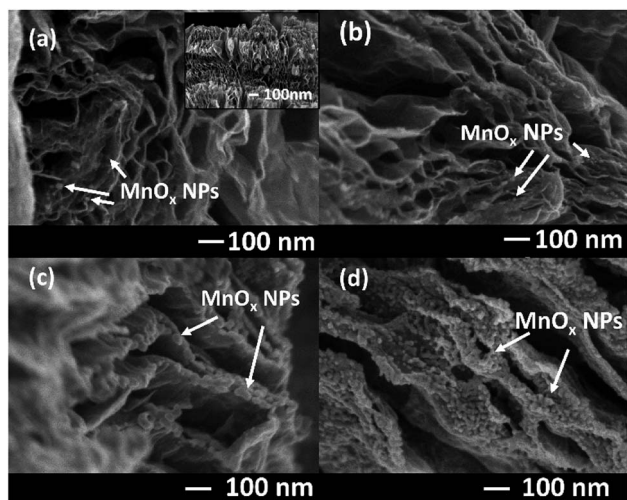


Fig. 1 FE-SEM images of $\text{MnO}_x/\text{rGO}_{\text{ae}}$ with different GO : KMnO_4 precursor weight ratios including (a) 8 : 1, (b) 4 : 1, (c) 2 : 1, and (d) 1 : 1.

MnO_x particle size increases with increasing Mn source. The size of the nanoparticles is in the range of ~ 10 to 50 nm.

The elemental composition of $\text{MnO}_x/\text{rGO}_{\text{ae}}$ can be confirmed using the EDS technique. The EDS spectra (see Fig. S1†) show the C, O, Mn elements. The at.% of Mn increases with the increasing amount of Mn precursor. For instance, 2.5% and 6.1% of Mn were quantified for 8 : 1 and 1 : 1 GO : KMnO_4 , respectively. Also, the residual K element can be observed in the composite. In fact, it will not affect the electrochemical performance of the supercapacitor as it can be considered as a kind of K-intercalated MnO_x .

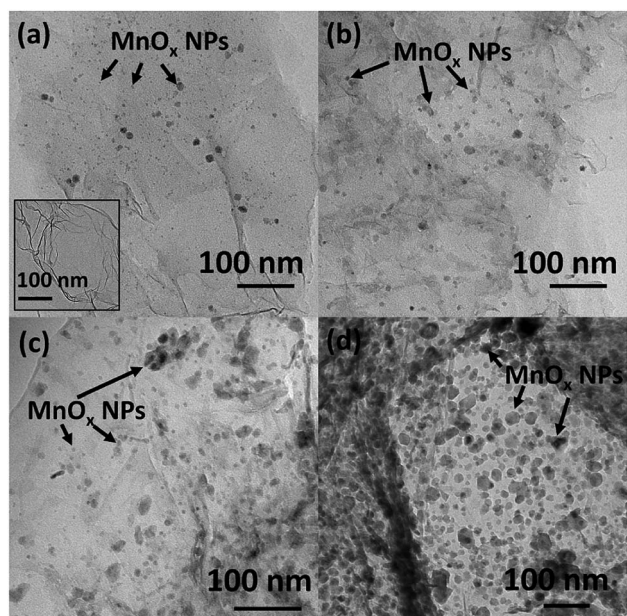


Fig. 2 TEM images of $\text{MnO}_x/\text{rGO}_{\text{ae}}$ with different GO : KMnO_4 precursor ratios including (a) 8 : 1, (b) 4 : 1, (c) 2 : 1, and (d) 1 : 1 wt%.

To further investigate the morphology of samples, TEM images are presented in Fig. 2. The number of MnO_x nanoparticles decorated on the rGO sheet increases with increasing Mn precursor. The MnO_x nanoparticles are in the range of 10 – 30 nm for low content of KMnO_4 precursor. At higher KMnO_4 precursor content, the particle sizes of MnO_x NPs are 10 – 50 nm. It corresponds with FE-SEM measurement.

The XRD patterns of the GO_{ae} , rGO_{ae} , and $\text{MnO}_x/\text{rGO}_{\text{ae}}$ composites are shown in Fig. 3a. The XRD pattern for GO_{ae} shows a characteristic peak at around 10° , corresponding to the (001) plane of graphene oxide. After the reduction of GO_{ae} by the microwave method, rGO_{ae} shows the broad peak at around 25.8° which is attributed to an (002) plane of graphitic carbon materials. It indicates the effective reduction of the oxygen-functional group on the GO_{ae} structure by microwave method. For $\text{MnO}_x/\text{rGO}_{\text{ae}}$ composites, the mixed phase of MnO and Mn_3O_4 and residual GO are observed.⁵

The FTIR spectroscopy was used to identify functional groups of the rGO_{ae} and $\text{MnO}_x/\text{rGO}_{\text{ae}}$ composite. The FTIR spectra (Fig. 3b) show three peaks at 1610 , 1216 , and 1132 cm^{-1} which can be referred to the remaining C=C, C-O, and C-OH, respectively.²⁸ Additionally, $\text{MnO}_x/\text{rGO}_{\text{ae}}$ composites exhibit two characteristic peaks at 492 and 614 cm^{-1} which can be attributed to Mn-O stretching.¹⁰

Fig. 3c shows the Raman spectra of the as-synthesized materials showing D and G bands at 1360 and 1598 cm^{-1} , respectively. D band corresponds to the disordered structure or defect (sp^3 carbon), while the G band relates to the ordered structure (sp^2) of carbon material. The intensity ratio of D to G band (I_D/I_G) can be

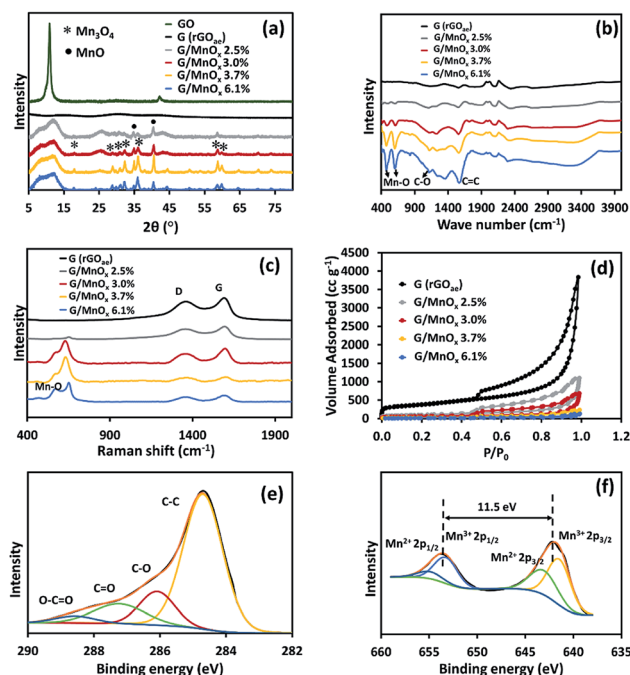


Fig. 3 (a) XRD patterns, (b) FTIR spectra, (c) Raman spectra, (d) nitrogen adsorption/desorption isotherm, (e) XPS C 1s spectrum, and (f) XPS Mn 2p spectrum of $\text{MnO}_x/\text{rGO}_{\text{ae}}$ composite at the Mn content of 3.7 at%.



used to evaluate the sp^2 domain size and degree of the disorder of the graphene-based materials. The I_D/I_G ratio of rGO_{ae} is 0.84, while the MnO_x/rGO_{ae} composites exhibit lower ratios in the range of 0.6–0.8 due to MnO_x formation reaction decreases the surface defects.²⁹ In addition, MnO_x/rGO_{ae} composites peaks at 577 and 649 cm^{-1} are attributed to MnO .⁶

The nitrogen adsorption/desorption isotherms of rGO_{ae} and MnO_x/rGO_{ae} composites are shown in Fig. 3d. Type-IV isotherms were obtained for all samples.³⁰ The specific surface areas of rGO_{ae} and MnO_x/rGO_{ae} with different Mn contents of 2.5, 3.0, 3.7, and 6.1 at% are 1279, 352, 200, 70, and 34 $m^2 g^{-1}$, respectively. The total pore volume of MnO_x/rGO_{ae} decreases with increasing Mn content, which is 1.69, 1.02, 0.34, and 0.17 $cm^3 g^{-1}$, respectively. Whilst, the total pore volume of rGO_{ae} is 5.80 $cm^3 g^{-1}$. The average pore diameters of rGO_{ae} and MnO_x/rGO_{ae} with Mn content of 2.5, 3.0, 3.7, and 6.1 at% are 21.2, 19.1, 20.5, 19.2, 20.6 nm, respectively.

XPS was carried to confirm the incorporation of MnO_x on the graphene sheet. The XPS results of MnO_x/rGO_{ae} composite with 3.7 at% Mn is shown in Fig. 3e and f. The C 1s spectrum can be deconvoluted into four peaks at 284.7, 286.1, 287.3, and 288.6 eV corresponding to the typical signals of C–C/C=C, C–O (hydroxyl and epoxy groups), C=O (carbonyl groups), and O–C=O (carboxyl groups),²⁹ respectively. Fig. 3f shows that the Mn 2p_{3/2} and Mn 2p_{1/2} of the MnO_x in the composite exhibit the binding energies at 642.1 eV and 653.6 eV, respectively. The energy separation is 11.5 eV which is in good agreement for Mn_3O_4 .³¹

CV and GCD were used to measure the electrochemical performance of symmetrical supercapacitors with different MnO_x/rGO_{ae} composites. The CV (Fig. 4a) and GCD (Fig. 4b and c) of supercapacitors were measured at a cell potential of 1.2 V in 1 M Na_2SO_4 electrolyte. Fig. 4a shows the CV curves of symmetrical rGO_{ae} and MnO_x/rGO_{ae} supercapacitors at a scan rate of 10 $mV s^{-1}$ which show nearly rectangular shape. The specific capacitance (Fig. 4d) was calculated from the GCD as the following eqn (1):³²

$$C_s = 4C_{cell} = 4 \left(\frac{I \Delta t}{m \Delta V} \right) \quad (1)$$

where I is the discharging current ($A g^{-1}$), Δt is the discharging time (s), ΔV is the potential (V), and m is the total mass of active materials in positive and negative electrodes of the full cell. The plot of the specific capacitance vs. the specific current for rGO_{ae} and MnO_x/rGO_{ae} composites is shown in Fig. 4d. The symmetric MnO_x/rGO_{ae} devices show higher specific capacitances than bare rGO_{ae} . Among the composites, the higher specific capacitance of 240 $F g^{-1}$ at a specific current of 0.5 $A g^{-1}$ was measured for MnO_x/rGO_{ae} with a Mn content of 3.0 at% as compared to that of other samples. Also, the measured specific capacitance is higher than the reported systems in the literature (Table 1). The maximum cell potential of 0.9 V with an excellent capacitance retention of 90% was estimated after 10 000 cycles at a specific current of 2.0 $A g^{-1}$ (Fig. 4e). Note, all electrochemical evaluation was operated at ca. 100% coulombic and energy efficiencies (see Fig. 4e).

The specific energy and specific power can be calculated from the following equation:

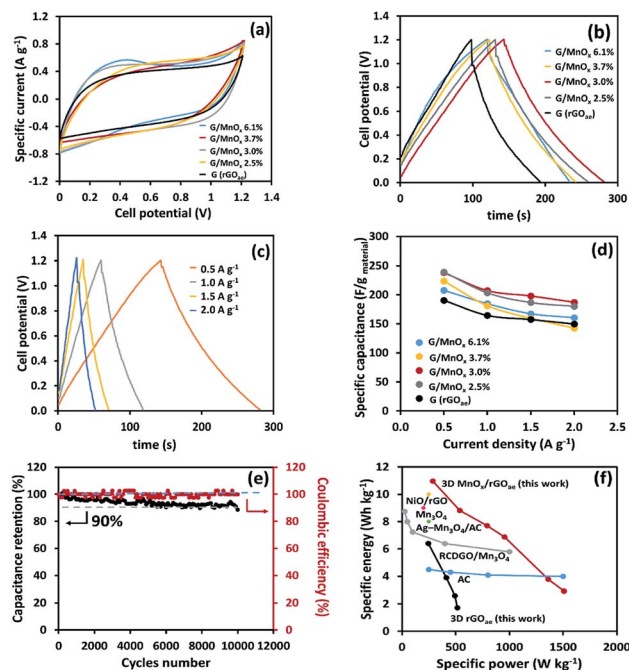


Fig. 4 (a) CV curves at a scan rate of 10 $mV s^{-1}$, (b) GCD curves at a specific current of 0.5 $A g^{-1}$ of symmetric supercapacitors based on rGO_{ae} and MnO_x/rGO_{ae} , (c) GCD curves at specific currents from 0.5 to 2.0 $A g^{-1}$, (d) the specific capacitances of rGO_{ae} and MnO_x/rGO_{ae} , (e) cycling performance of symmetric supercapacitor based on MnO_x/rGO_{ae} at a Mn content of 3.0 at% at a specific current of 2.0 $A g^{-1}$, and (f) Ragone plot as compared to other previous work.

$$E = \frac{1}{2} C_{cell} \Delta V^2 \quad (2)$$

$$P = \frac{E}{t} \quad (3)$$

where E is the specific energy, C_{cell} is the capacitance of full cell, ΔV is the potential excluding the IR drop, P is the specific power, and t is the discharging time. The Ragone plot of symmetric supercapacitor with rGO_{ae} and its composites is shown in Fig. 4f. The MnO_x/rGO_{ae} with a Mn content of 3.0 at% shows the highest specific energy of 10.9 $W h kg^{-1}$ and a specific power of 286 $W kg^{-1}$. The measured values are higher than those of the similar reported symmetric supercapacitors in the literature.^{33–36}

The CV and EQCM results of the MnO_x/rGO_{ae} at a Mn content of 3.0 at% in 1.0 M Na_2SO_4 (aq.) at a scan rate of 10 $mV s^{-1}$ are shown in Fig. 5. The quartz resonance frequency (Δf) related to mass change of electrode (Δm) by Sauerbrey's equation:³⁷

$$\Delta m = -C_f \Delta f \quad (4)$$

where C_f is a calibration constant ($0.0815 \text{ Hz ng}^{-1} \text{ cm}^2$).³⁸ Note that, the negative frequency response ($-\Delta f$) increases with increasing the electrode mass (Δm).

To study the anion and cation contribution, the data were collected at two different potential ranges; positive and negative



Table 1 The comparison of the specific capacitance of 3D MnO_x/rGO_{ae} (Mn = 3.0%) electrode with the reported graphene/MnO_x composites using the 3-electrode configuration

Material	Specific capacitance	Electrolyte	Ref.
Graphene/Mn ₃ O ₄	121 F g ⁻¹ at 0.5 A g ⁻¹	1 M Na ₂ SO ₄	13
Graphene/Mn ₃ O ₄	225 F g ⁻¹ at 5 mV s ⁻¹	1 M Na ₂ SO ₄	10
Graphene sheet/Mn ₃ O ₄	181 F g ⁻¹ at 0.2 A g ⁻¹	1 M Na ₂ SO ₄	39
Graphene/Mn ₃ O ₄	193 F g ⁻¹ at 0.05 A g ⁻¹	Na ₂ SO ₄ (sat.)	15
Graphene/Mn ₃ O ₄	192 F g ⁻¹ at 0.5 A g ⁻¹	K ₂ SO ₄ (sat.)	40
rGO/Mn ₃ O ₄ nanorods	176 F g ⁻¹ at 1.0 A g ⁻¹	1 M Na ₂ SO ₄	41
rGO/Mn ₃ O ₄ nanocomposite	160 F g ⁻¹ at 0.5 A g ⁻¹	1 M Na ₂ SO ₄	6
Graphene oxide double-shell hollow spheres/ Mn ₃ O ₄	225 F g ⁻¹ at 5 mV s ⁻¹	0.5 M Na ₂ SO ₄	29
rGO/Mn ₃ O ₄	186 F g ⁻¹ at 0.25 A g ⁻¹	1 M Na ₂ SO ₄	42
rGO/Mn ₃ O ₄	194 F g ⁻¹ at 0.5 A g ⁻¹	1 M Na ₂ SO ₄	43
Graphene/Mn ₃ O ₄ nanocrystalline	260 F g ⁻¹ at 0.25 A g ⁻¹	1 M Na ₂ SO ₄	44
rGO/Mn ₃ O ₄	195 F g ⁻¹ at 1.0 A g ⁻¹	1 M Na ₂ SO ₄	45
Graphene–Mn ₃ O ₄	247 F g ⁻¹ at 5 mV s ⁻¹	K ₂ SO ₄ (sat.)	46
Porous graphene/Mn ₃ O ₄	208 F g ⁻¹ at 0.5 A g ⁻¹	1 M Na ₂ SO ₄	47
3D MnO _x /rGO aerogel	238 F g ⁻¹ at 0.5 A g ⁻¹	1 M Na ₂ SO ₄ (2-electrode system)	This work
	266 F g ⁻¹ at 0.5 A g ⁻¹	1 M Na ₂ SO ₄	

potential ranges. In Fig. 5a, the CV is started at the potential from 0.10 V to −1.00 V vs. Ag/AgCl. The opposite frequency response (−Δf) simultaneously increases implying that the electrode mass (Δm) increases owing to the adsorption of solvated Na⁺ ions. During the reverse scan from −1.00 to 0.07 V vs. Ag/AgCl, the mass change of the electrode decreases due to the desorption of solvated Na⁺. Between 0.05 and 0.25 V vs. Ag/AgCl in the positive sweep, the mass change of the electrode is almost the same because of the desorption of the solvated cations and adsorption of the solvated anion in the electrode surface. It is due to the double layer consisting solvated cations and anions at a zero charge potential.⁴⁸ Further increment of potential up to 0.6 V results the steep increase of Δm due to the adsorption of solvated SO₄^{2−} ions.⁴⁹ Thereafter, a steady increment of Δm is noted up to the 0.9 V and the reduction of Δm is observed from 0.9 to 1.0 V. These changes cannot be explained based on the pure ion sorption process as it only increases the mass of the electrode. In this potential region, possibly the redox reaction of MnO_x occurs⁴⁹ along with the ion adsorption process. The former decreases the mass, while the latter increases the mass of the electrode. The mass change as a result of anion adsorption is the dominant process over the redox

reaction of MnO_x in the potential range of 0.6 to 0.9 V, which results in a steady increment of the electrode mass. While the dissolution process becomes a major role, thereafter, leading to the reduction of mass up to 1.0 V. On the reverse scan, the mass decreases steadily up to 0.05 V due to the desorption of the anion. A small increment of mass is noted at 0.65 V is possibly due to the redox reaction of MnO_x.⁴⁹ The mass changes in positive and negative potential ranges are 18 and 11 ng cm^{−2}. The anion is adsorbed on the MnO_x/rGO_{ae} surface with *ca.* 1.7 times higher than the cation adsorption.

DEMS was used for the *in situ* gas evolution analysis of symmetrical supercapacitors using the MnO_x/rGO_{ae} composite during the CV measurement. Fig. 6 shows the gas evolution profile. The CO₂ evolution starts at a cell potential of 1.0 V and above, possibly due to the carbon corrosion and the subsequent oxidation of corrosion product as a result of the oxygen evolution at the positive electrode (eqn(5)–(8)).⁵⁰ It agrees well with the maximum cell potential identified by the long-term stability measurement. Initially, the oxygen/hydroxyl radicals generated at the carbon electrodes react with carbon leading to CO and CO₂. The detection of CO₂ alone indicates the further oxidation of CO into CO₂.⁵⁰

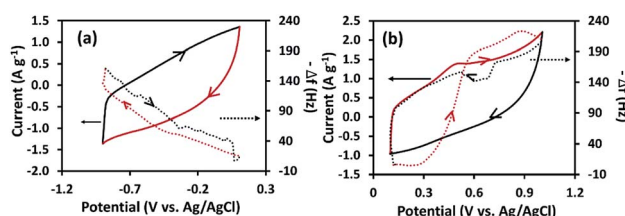


Fig. 5 CVs and EQCM frequency response of MnO_x/rGO_{ae} (3.0 at% Mn) at 10 mV s^{−1} in 1.0 M Na₂SO₄ (aq.) electrolyte in three electrode systems at (a) negative and (b) positive potential scans. Note that dashed lines present the frequency responses and solid lines present the CV response. Red and black curves represent charge and discharge of ions, respectively.

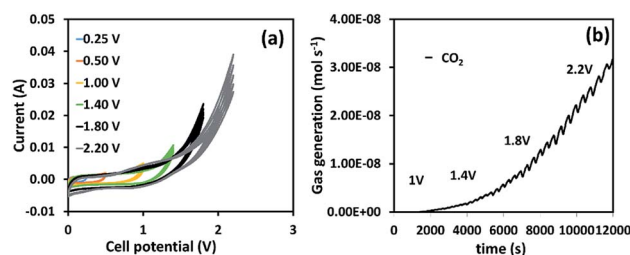
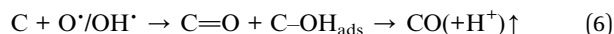
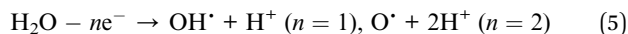


Fig. 6 (a) CVs of the symmetrical supercapacitor of MnO_x/rGO_{ae} (3.0 at% Mn) at 10 mV s^{−1} with different cell potential intervals and (b) CO₂ evolution profile during CV measurement.





Conclusion

The symmetric neutral electrochemical capacitor of $\text{MnO}_x/\text{rGO}_{\text{ae}}$ composites synthesised by a chemical and microwave synthesis exhibits a specific capacitance of 240 F g^{-1} at a specific current of 0.5 A g^{-1} , a maximum specific energy of 10.9 W h kg^{-1} and a specific power of 286 W kg^{-1} in $1.0 \text{ M Na}_2\text{SO}_4$ (aq.). The cycling stability of 90% was measured after 10 000 cycles at a cell potential of 0.9 V. In addition, the charge storage mechanism was investigated by electrochemical quartz crystal microbalance (EQCM), demonstrating the ion adsorption/desorption process and the dissolution of MnO_x from $\text{MnO}_x/\text{rGO}_{\text{ae}}$. DEMS measurement shows CO_2 evolution at 1.0 V, which validates the identified maximum cell potential by the long-term stability test. Also, the detection of CO_2 hints that the positive electrode possibly limits the cell potential. This finding will be useful for further development of practical high power and energy storage devices.

Conflicts of interest

There are no conflicts to declare.

Acknowledgements

This work was financially supported by the Vidyasirimedhi Institute of Science and Technology and Thailand Research Fund (RSA6180031 and RTA6080005) as well as Energy Policy and Planning Office (EPPO), Ministry of Energy, Thailand. Support from the Frontier Research Centre at VISTEC is also acknowledged.

References

- 1 P. Yang and W. Mai, *Nano Energy*, 2014, **8**, 274–290.
- 2 D. Zhou, H. Lin, F. Zhang, H. Niu, L. Cui, Q. Wang and F. Qu, *Electrochim. Acta*, 2015, **161**, 427–435.
- 3 J. Yang, X. Yang, Y. L. Zhong and J. Y. Ying, *Nano Energy*, 2015, **13**, 702–708.
- 4 D. Zhang, Y. Zhang, Y. Luo and P. K. Chu, *Nano Energy*, 2015, **13**, 47–57.
- 5 X. Zhao, Y. Du, Y. Li and Q. Zhang, *Ceram. Int.*, 2015, **41**, 7402–7410.
- 6 X. She, X. Zhang, J. Liu, L. Li, X. Yu, Z. Huang and S. Shang, *Mater. Res. Bull.*, 2015, **70**, 945–950.
- 7 R. Peng, N. Wu, Y. Zheng, Y. Huang, Y. Luo, P. Yu and L. Zhuang, *ACS Appl. Mater. Interfaces*, 2016, **8**, 8474–8480.
- 8 B. G. S. Raj, R. N. R. Ramprasad, A. M. Asiri, J. J. Wu and S. Anandan, *Electrochim. Acta*, 2015, **156**, 127–137.
- 9 V. Hiremath, M. Cho and J. G. Seo, *New J. Chem.*, 2018, **42**, 19608–19614.
- 10 Y. Wu, S. Liu, H. Wang, X. Wang, X. Zhang and G. Jin, *Electrochim. Acta*, 2013, **90**, 210–218.
- 11 H. Fei, C. Yang, H. Bao and G. Wang, *J. Power Sources*, 2014, **266**, 488–495.
- 12 H. Tang, Y. J. Zhang, Q. Q. Xiong, J. D. Cheng, Q. Zhang, X. L. Wang, C. D. Gu and J. P. Tu, *Electrochim. Acta*, 2015, **156**, 86–93.
- 13 J. W. Lee, A. S. Hall, J.-D. Kim and T. E. Mallouk, *Chem. Mater.*, 2012, **24**, 1158–1164.
- 14 S. Yang, X. Song, P. Zhang and L. Gao, *J. Mater. Chem. A*, 2013, **1**, 14162–14169.
- 15 Q. Jiangying, G. Feng, Z. Quan, W. Zhiyu, H. Han, L. Beibei, W. Wubo, W. Xuzhen and Q. Jieshan, *Nanoscale*, 2013, **5**, 2999–3005.
- 16 W. Zhang, Z. Chen, X. Guo, K. Jin, Y. Wang, L. Li, Y. Zhang, Z. Wang, L. Sun and T. Zhang, *Electrochim. Acta*, 2018, **278**, 51–60.
- 17 H. Banda, D. Aradilla, A. Benayad, Y. Chenavier, B. Daffos, L. Dubois and F. Duclairoir, *J. Power Sources*, 2017, **360**, 538–547.
- 18 Y. Tan, D. Wu, T. Wang, P. Liu, J. Guo and D. Jia, *Appl. Surf. Sci.*, 2018, **455**, 683–695.
- 19 L. Wang, X. Ye, P. Zhao, H. Jiang, Y. Zhu, Z. Wan, G. Rao, S. You, G. Zeng and J. Fu, *Appl. Surf. Sci.*, 2019, **467**, 949–953.
- 20 Q. Zhang, Y. Wang, B. Zhang, K. Zhao, P. He and B. Huang, *Carbon*, 2018, **127**, 449–458.
- 21 M. Yang, K. G. Lee, S. J. Lee, S. B. Lee, Y.-K. Han and B. G. Choi, *ACS Appl. Mater. Interfaces*, 2015, **7**, 22364–22371.
- 22 R. Kumar, R. K. Singh, A. R. Vaz, R. Savu and S. A. Moshkalev, *ACS Appl. Mater. Interfaces*, 2017, **9**, 8880–8890.
- 23 T. Liu, H. Chai, D. Jia, Y. Su, T. Wang and W. Zhou, *Electrochim. Acta*, 2015, **180**, 998–1006.
- 24 X. Xu, J. Shen, N. Li and M. Ye, *J. Alloys Compd.*, 2014, **616**, 58–65.
- 25 W. He, H. Qiu, J. Meng, B. Liu, J. Cui and Y. Zhang, *J. Alloys Compd.*, 2019, **788**, 183–190.
- 26 M. Sawangphruk, P. Srimuk, P. Chiochan, A. Krittayavathananon, S. Luanwuthi and J. Limtrakul, *Carbon*, 2013, **60**, 109–116.
- 27 B. Patil, S. Ahn, S. Yu, H. Song, Y. Jeong, J. H. Kim and H. Ahn, *Carbon*, 2018, **134**, 366–375.
- 28 G. S. Gund, D. P. Dubal, B. H. Patil, S. S. Shinde and C. D. Lokhande, *Electrochim. Acta*, 2013, **92**, 205–215.
- 29 C. Zhang, L. Wang, Y. Zhao, Y. Tian and J. Liang, *Carbon*, 2016, **107**, 100–108.
- 30 Z. Lin, G. H. Waller, Y. Liu, M. Liu and C.-p. Wong, *Carbon*, 2013, **53**, 130–136.
- 31 L. Zhang, L. Zhao and J. Lian, *RSC Adv.*, 2014, **4**, 41838–41847.
- 32 H. Cao, X. Peng, M. Zhao, P. Liu, B. Xu and J. Guo, *RSC Adv.*, 2018, **8**, 2858–2865.
- 33 S. Nagamuthu, S. Vijayakumar and G. Muralidharan, *Dalton Trans.*, 2014, **43**, 17528–17538.



- 34 F. Gao, J. Qu, Z. Zhao, Q. Zhou, B. Li and J. Qiu, *Carbon*, 2014, **80**, 640–650.
- 35 X.-J. Ma, W.-B. Zhang, L.-B. Kong, Y.-C. Luo and L. Kang, *RSC Adv.*, 2015, **5**, 97239–97247.
- 36 A. A. Yadav, S. Jadhav, D. Chougule, P. Patil, U. Chavan and Y. Kolekar, *Electrochim. Acta*, 2016, **206**, 134–142.
- 37 W.-Y. Tsai, P.-L. Taberna and P. Simon, *J. Am. Chem. Soc.*, 2014, **136**, 8722–8728.
- 38 A. Krittayavathananon, T. Pettong, P. Kidkhunthod and M. Sawangphruk, *Electrochim. Acta*, 2017, **258**, 1008–1015.
- 39 L. Li, K. H. Seng, H. Liu, I. P. Nevirkovets and Z. Guo, *Electrochim. Acta*, 2013, **87**, 801–808.
- 40 F. Gao, J. Qu, Z. Zhao, Q. Zhou, B. Li and J. Qiu, *Carbon*, 2014, **80**, 640–650.
- 41 Y. Liu, W. Wang, Y. Wang, Y. Ying, L. Sun and X. Peng, *RSC Adv.*, 2014, **4**, 16374–16379.
- 42 J. Xu, X. Fan, Q. Xia, Z. Shao, B. Pei, Z. Yang, Z. Chen and W. Zhang, *J. Alloys Compd.*, 2016, **685**, 949–956.
- 43 Y. Wang, Z. Ji, X. Shen, K. Xu and A. Yuan, *J. Alloys Compd.*, 2016, **684**, 366–371.
- 44 X. Yang, Y. He, Y. Bai, J. Zhang, L. Kang, H. Xu, F. Shi, Z. Lei and Z.-H. Liu, *Electrochim. Acta*, 2016, **188**, 398–405.
- 45 P. Rosaiah, J. Zhu, D. P. Shaik, O. Hussain, Y. Qiu and L. Zhao, *J. Electroanal. Chem.*, 2017, **794**, 78–85.
- 46 Y. Long, J. Xie, H. Li, Z. Liu and Y. Xie, *J. Solid State Chem.*, 2017, **256**, 256–265.
- 47 T. Wang, Q. Le, X. Guo, M. Huang, X. Liu, F. Dong, J. Zhang and Y. X. Zhang, *ACS Sustainable Chem. Eng.*, 2018, **7**, 831–837.
- 48 J. M. Griffin, A. C. Forse, H. Wang, N. M. Trease, P.-L. Taberna, P. Simon and C. P. Grey, *Faraday Discuss.*, 2015, **176**, 49–68.
- 49 Q. Li, J. M. Anderson, Y. Chen and L. Zhai, *Electrochim. Acta*, 2012, **59**, 548–557.
- 50 M. He, K. Fic, E. Fra, P. Novák and E. J. Berg, *Energy Environ. Sci.*, 2016, **9**, 623–633.

